25-Second Determination of 2019 M_w 7.1 Ridgecrest Earthquake Coseismic Deformation

Timothy I. Melbourne*[1], Walter M. Szeliga[1], V. Marcelo Santillan[1], and Craig W. Scrivner[1]

ABSTRACT

We have developed a global earthquake monitoring system based on low-latency measurements from more than 1000 existing Global Navigational Satellite System (GNSS) receivers, of which nine captured the 2019 M_w 6.4 Ridgecrest, California, foreshock and M_w 7.1 mainshock earthquakes. For the foreshock, coseismic offsets of up to 10 cm are resolvable on one station closest to the fault, but did not trigger automatic offset detection. For the mainshock, GNSS monitoring determined its coseismic deformation of up to 70 cm on nine nearby stations within 25 s of event nucleation. These 25 s comprise the fault rupture duration itself (roughly 10 s of peak moment release), another 10 s for seismic waves and displacement to propagate to nearby GNSS stations, and a few additional seconds for surface waves and other crustal reverberations to dissipate sufficiently such that coseismic offset estimation filters could reconverge. Latency between data acquisition in the Mojave Desert and positioning in Washington State averaged 1.4 s, a small fraction of the fault rupture time itself. GNSS position waveforms for the two closest stations that show the largest dynamic and static displacements agree well with postprocessed time series. Mainshock coseismic ground deformation estimated within 25 s of origin time also agrees well with, but is ~10% smaller than, deformation estimated using 48 hr observation windows, which may reflect rapid postseismic fault creep or the cumulative effect of nearly 1000 aftershocks in the 48 hr following the mainshock. GNSS position waveform shapes, which comprise a superposition of dynamic and static displacements, are well modeled by frequency–wavenumber synthetics for the Hadley–Kanamori 1D crustal structure model and the U.S. Geological Survey finite-rupture distribution and timing. These results show that GNSS seismic monitoring performed as designed and offers a new means of rapidly characterizing large earthquakes globally.

KEY POINTS

- Real-time GNSS positioning measured the Ridgecrest M 7.1 mainshock coseismic deformation in under 30 s.
- Real-time position waveforms and coseismic offsets match predicted and post-processed estimates.
- GNSS ultrafast characterization of earthquake deformation and magnitude is shown to work well.

Supplemental Material

INTRODUCTION

Over the past century, seismic networks comprising inertial velocity seismometers and strong ground motion accelerometers have provided the primary source of rapid earthquake characterization that inform first responders, tsunami warnings for coastal events, and early warning systems such as ShakeAlert (Hutton *et al.*, 2010; Kong *et al.*, 2015; Given *et al.*, 2018). Algorithms that pick and correlate seismic phases to rapidly compute hypocenters and local magnitude are mature, time-tested, and routinely used to inform downstream models of impact such as ShakeCast and ShakeMap (Wald *et al.*, 1999, 2008). However, many observations of complex seismic rupture spanning multiple faults have repeatedly demonstrated the saturation and source-coda ambiguity limitations inherent to using only local seismic networks to rapidly characterize large earthquake magnitude and rupture extent (e.g., Litchfield *et al.*, 2018; Ross *et al.*, 2019). Regional or teleseismic waveforms offer better constraints, but at the cost of travel-time delays that reach into tens of minutes. Global Navigational Satellite System (GNSS, of which Global Positioning System [GPS] is the U.S. system) ground tracking networks offer a straightforward solution to this problem, and

1. Pacific Northwest Geodetic Array, Department of Geological Sciences, Central Washington University, Ellensburg, Washington, U.S.A.

*Corresponding author: tim@geology.cwu.edu

Cite this article as Melbourne, T. I., W. M. Szeliga, V. Marcelo Santillan, and C. W. Scrivner (2020). 25-Second Determination of 2019 M_w 7.1 Ridgecrest Earthquake Coseismic Deformation, *Bull. Seismol. Soc. Am.* **110**, 1680–1687, doi: 10.1785/0120200084

have been increasingly used to fortify regional seismic monitoring in generating quick and accurate magnitude estimates for large local earthquakes (Hudnut *et al.*, 2002; Grapenthin *et al.*, 2014a,b). With their ongoing global proliferation, real-time GNSS positioning now offers a complementary means of rapidly characterizing large earthquakes.

First, because near-field (static) deformation grows linearly with respect to moment, GNSS position measurements made in general proximity to a rupturing fault and computed in real time can measure ground deformation as it evolves. This, in turn, can be directly related to ongoing moment release without requiring specific knowledge of focal mechanism, rupture depth, or spatial extent of rupture, using simple scaling relationships that relate expected coseismic offset to moment as a function of station-faulting distance (Crowell *et al.*, 2013). Where station density permits doing so, the spatial extent and characteristics of distributed slip may also be determined, and done so far faster than teleseismic or even regional *W*-phase analyses permit (Minson *et al.*, 2014; Crowell *et al.*, 2016). Other hybrid approaches are also possible, for instance combining GNSS-constrained coseismic offsets with seismic first-motion focal mechanisms to better estimate moment. Second, although near-field deformation measurements are most useful for rapidly constraining seismogenic rupture, in practice, the majority of GNSS stations around the globe have been built as regional or national dual-use land surveying networks. As a result, many stations are concentrated in the vicinity of populated areas where they offer the most potential for characterizing large local or regional earthquakes far more quickly than teleseismic analyses can.

The purpose of this article is to illustrate the utility, accuracy, and limitations of real-time GNSS positioning for the purpose of seismic monitoring and rapid local earthquake characterization. We compare GNSS position time series generated in real time from the 2019 Ridgecrest foreshock and mainshock earthquakes (Barnhart *et al.*, 2019; Ross *et al.*, 2019) with postprocessed time series as well as modeled synthetic time series generated from a purely seismometer-based inversion for the finite-fault source and the standard crustal structure model for southern California. Here, "real time" means within 1.5 s of actual time, and all real-time positions shown were generated with less than 1.5 s of latency between raw satellite observables acquisition in the Mojave Desert of eastern California and the generation of a full solution (instantaneous position estimate plus covariances) at Central Washington University (CWU) located ~1300 km north in Washington State. Positioning in real time is challenging compared with postprocessing GNSS data, because it requires that precise corrections to broadcast satellite clocks and orbits be incorporated into position estimation to account for time-dependent noise sources (satellite clock drift, solar wind, and so forth). Real-time positioning thus requires simultaneously streaming in both raw GNSS satellite observables as well as a variety of ancillary products continuously generated from separate, usually global, analyses. By contrast, in traditional postprocessing of GNSS data, more accurate "final" satellite clock, orbit, and other ancillary products determined with several weeks' latency using multiday orbit analyses, are employed through static files in station position estimation. All time series and coseismic offset estimates discussed here are included in the supplemental material available to this article.

In Figures 1–3, we validate CWU real-time GNSS station position time series and the coseismic offsets estimated from them using independently generated postprocessed time series and offset estimates. The postprocessed time series were generated by D. Mencin of UNAVCO, Inc. (Mattioli *et al.*, 2020), whereas the mainshock coseismic offsets were estimated following the standard Geodesy Advancing Geosciences and EarthScope (GAGE) earthquake deformation estimation procedure that employs 48 hr of data before and after an event, as described in Herring *et al.* (2016). Agreement between the two data sets is generally good; the real-time dynamic waveforms generally closely match the postprocessed. Moreover, coseismic offsets estimated within 25 s of origin time largely agree with, although are roughly 10% smaller than, offsets estimated using 48 hr data windows (Fig. 2). Much of this discrepancy may ultimately prove to be real, reflecting extra deformation in the 48 hr following the mainshock caused by rapid fault-zone afterslip and/or the cumulative deformation of nearly 1000 aftershocks over the 48 hr following the mainshock, 71 of which were magnitude 4.0 or higher. Finally, the seismic phase absolute arrival times, amplitudes, and overall shapes observed in the real-time GNSS position time series (Fig. 4) are well modeled by synthetic seismograms generated using frequency–wavenumber (f-k) Green's functions (Zhu and Rivera, 2002) for the standard southern California crustal model (Hadley and Kanamori, 1977; Hutton *et al.*, 2010) and the U.S. Geological Survey (USGS) mainshock finite-fault rupture distribution and timing (Hayes, 2017). This multipronged validation shows that the real-time system performed as designed during the mainshock event. As GNSS networks continue to expand globally, their observations open a new pipeline of analysis tools that complement many of the known challenges inherent to using only local seismic networks to rapidly characterize large local earthquakes.

GNSS POINT POSITIONING

During both the 4 July 2019 M_w 6.4 foreshock and 6 July 2019 M_w 7.1 Ridgecrest, California, earthquakes, roughly 700 stations from the Network of the Americas (NOTA) operated by UNAVCO, Inc. (Hodgkinson *et al.*, 2018) were being positioned in real time at CWU. Figure 1 shows position time series for 2 min around the origin time of the M_w 7.1 mainshock, as they were available in real time with no subsequent alteration. For comparison, east time series for the M_w 6.4 foreshock are also shown in the shaded box with the same time and

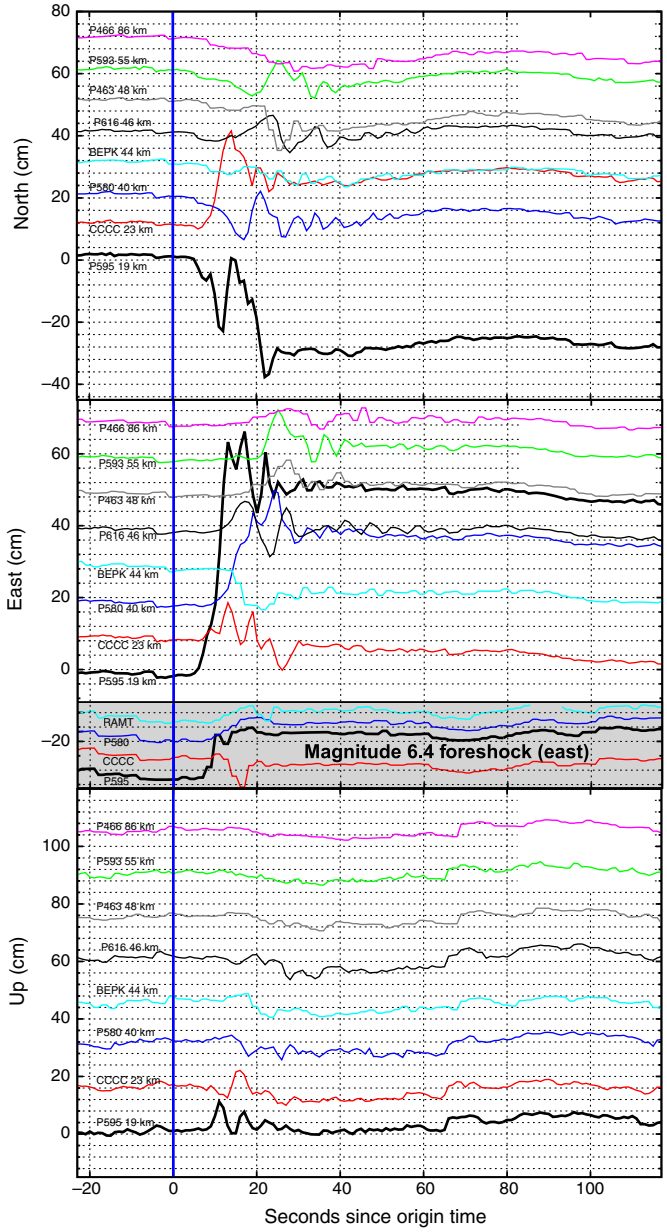

Figure 1. Global Navigational Satellite System (GNSS) International Terrestrial Reference Frame (ITRF14) precise point position (PPP) time series for the 6 July 2019 M_w 7.1 Ridgecrest mainshock, as estimated in real time at Central Washington University (CWU). Gray shaded box shows east–west component of positions for the four closest stations to the 4 July 2019 M_w 6.4 foreshock with origin time (OT) aligned to the M_w 7.1 and same time and position scale. Formal errors computed from Global Positioning System phase residuals are not shown for clarity but average 3, 4, and 5 cm in north, east, and vertical positions, respectively. Latency between satellite observation acquisition in the field and solution generated at CWU averaged 1.4 s for the hour around the mainshock event. The color version of this figure is available only in the electronic edition.

displacement axis scaling and with its origin time aligned to the mainshock. CWU estimates station precise point positions (PPP) with 1 s epochs in the 2014 International Terrestrial Reference Frame (ITRF14) (Altamimi *et al.*, 2011, 2016). ITRF14 is a global reference frame centered on the Earth's center of mass in which point positions in north, east, and vertical are determined independently of nearby stations. This approach contrasts with relative positioning with respect to a nearby single or group of regional stations assumed to be unmoving, as discussed by others (Zumberge *et al.*, 1997; Hudnut *et al.*, 2002; Grapenthin *et al.*, 2014a,b). Positions are estimated using GPS-only carrier phase observables and International GNSS Service (IGS) real-time corrections to broadcast satellite orbits and clocks (Dow *et al.*, 2009). Unlike other PPP algorithms (e.g., Kouba and Héroux, 2001) that rely on pseudorange, using only carrier phase greatly mitigates the influence of pseudorange multipath, and through its impact on carrier phase bias estimation, positioning accuracy. This, in turn, requires a continuous phase calibration, for which we use geometry-free linear combinations of L1 and L2 codes within a Kalman-filter to simultaneously estimate optimal floating point ambiguities while monitoring and correcting for cycle slips (Santillan *et al.*, 2013). Using only half the number of observables reduces the computational burden of position estimation, enables scaling to large numbers of GNSS stations on reasonable computational systems, and translates into smaller latencies. The resulting positions show typical root mean square scatter of 3 cm in the horizontal and 5 cm in the vertical, which peak in a 3–4 min frequency band (Melgar *et al.*, 2020). This dominant source of positioning error is traceable to a global wobble in the barycenter of the IGS clock corrections, and eliminating this 3–4 min wobble is the subject of ongoing research. For the purposes of seismic monitoring, however, at the periods of most crustal earthquake seismic phase frequencies (<1 min) present-day positioning noise is significantly less. Elimination of the 3–4 min noise source remains a top priority for the large earthquakes, typically subduction-zone events that do radiate significant power in the 3–4 min band. Average solution latency depends on telemetry type more than station location, globally, meaning data from New Zealand or Antarctic stations with good telemetry arrive at CWU with similar latencies as Washington State stations with good telemetry (meaning routing controls latency far more than distance divided by speed of light). The data set presented here has average latencies of under 1.5 s. Figure 2 (inset) shows the 2020 distribution of continuously operating GNSS receivers with real-time data telemetry operating along the mainland U.S. portion North American–Pacific plate boundary, all of which are continuously positioned at CWU.

COSEISMIC OFFSET ESTIMATION

We use a Kalman filter to estimate coseismic offsets from the GNSS position time series, and refer to this later as an "offset filter." GNSS point positions have time-dependent colored noise that originates from multiple physical processes that act over a wide range of time and spatial scales (Dong *et al.*,

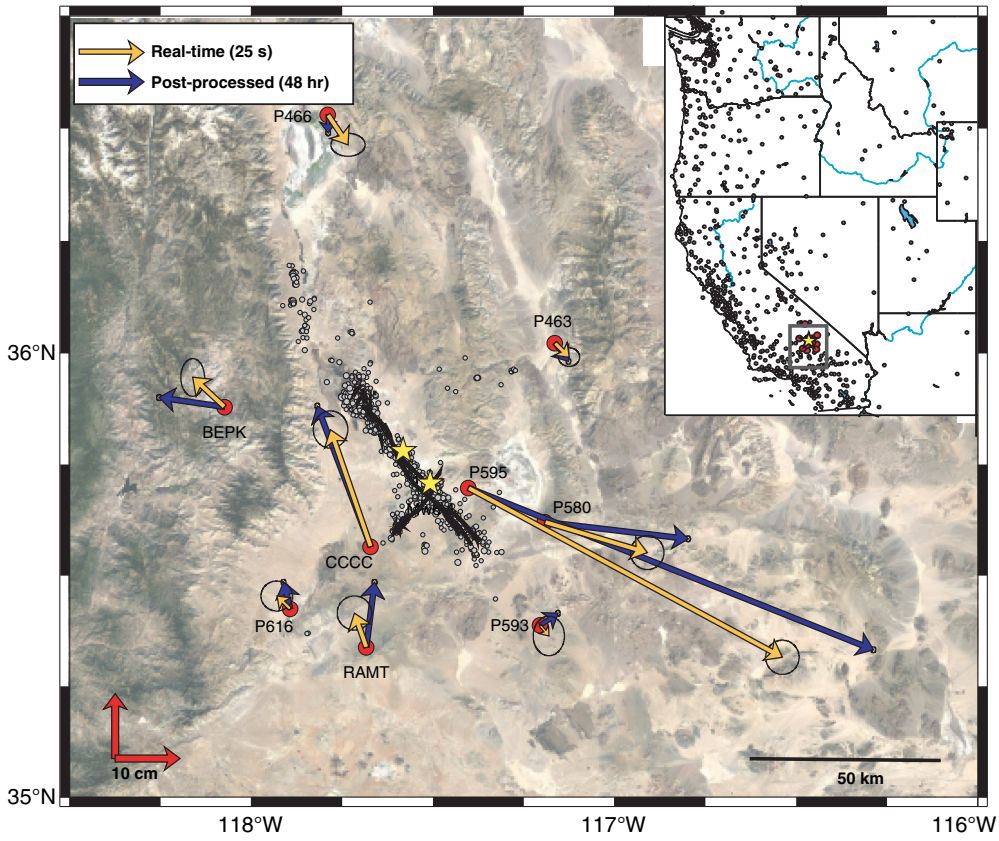

Figure 2. Comparison of coseismic offsets estimated from CWU real-time positions shown in Figure 1 at OT + 25 s (orange) versus postprocessing using position estimates based on 48 hr of data before and after the earthquakes (blue) following the GAGE methodology of Herring *et al.* (2016) and published in Mattioli *et al.* (2020). Mainshock coseismic deformation estimated within 25 s of OT at the nine Network of the Americas stations (red dots) closest to the fault zone are ~10% smaller than the 48 hr estimation. This may indicate rapid postseismic fault creep and/or the cumulative effect of nearly 1000 aftershocks, of which 71 events were M_w 4.0 or larger, over the 48 hr following the mainshock. Fault traces from Ponti *et al.* (2020). (Inset) Western U.S. real-time telemetered GNSS stations available for seismic monitoring in 2020. The color version of this figure is available only in the electronic edition.

2002). This complicates identifying and estimating coseismic offsets, much as background seismic noise complicates seismic phase picking. We model GNSS time series as stochastic processes comprising a constant plus time-variable, non-Gaussian, nonwhite noise, and we assume no correlation between stations or between components of a given station. This is the physically accurate model because the vast majority of time receivers are not physically moving within the ITRF14, apparent position wander is estimation noise, and coseismic deformation may result in any direction depending on an earthquake fault's orientation, rake, and location relative to the station. When positioning with 1 s epochs, we account for position wander through addition of process noise during filter update. We use the time-dependent statistics of the position time series, meaning both formal error of individual epochs as computed from postfit phase residuals, subsequently scaled by an additional time-dependent factor derived from the position scatter itself (usually greater than 1) to accommodate unmodeled noise not reflected in formal errors. In practice, this means noisier position time series degrades offset detectability of a given size within a given time window. Alternatively, it results in longer wait times until a given offset can be detected at some statistical threshold. This model is built into forward-only Kalman filters with time-dependent statistics designed to ignore drift and triggering on true coseismic motion while minimizing false positives and negatives, as discussed by Senko (2018).

Offset estimation filters are created and destroyed automatically by the real-time system as new GNSS station are introduced into CWU's global processing system or existing streams time out through any delay long enough to warrant a stochastic reset on the previous filter state. Dynamic displacements from the M_w 6.4 Ridgecrest foreshock did not trigger offset estimation because the positioning error prior to the event was sufficiently large that the largest coseismic offset, just under 10 cm on the east component of the closest station, was statistically insufficient to trigger the filter. This illustrates a practical lower limit to sparse-network detectability, currently roughly low- to mid-magnitude 6, depending on network geometry, although this magnitude is steadily dropping as improved global models enable lower-scatter positioning, with the ultimate goal of subcentimeter within a global reference frame (Melgar *et al.*, 2020). In contrast, the M_w 7.1 mainshock offsets triggered offset estimation filters that subsequently converged within 25 s, as timed by reconvergence interval following stochastic reset. At the nine NOTA stations closest to the fault zone, these agree well with, but are ~10% smaller than, the coseismic deformation estimated using postprocessed, 48 hr observation windows. These longer-latency offsets are estimated following the GAGE methodology of Herring *et al.* (2016) and published by UNAVCO, Inc., and can be considered the most accurate

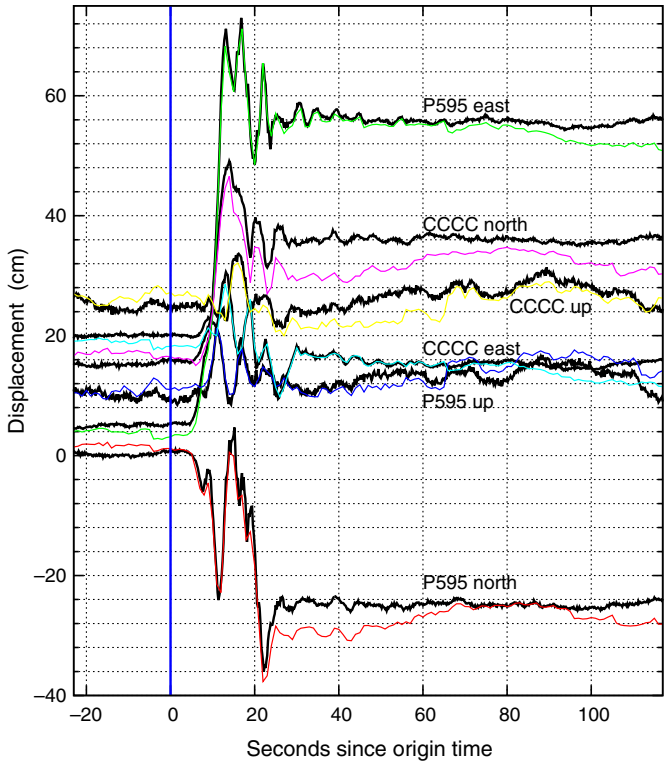

Figure 3. Comparison of real-time and postprocessed GNSS PPP north, east, and vertical (up) time series for M_w 7.1 Ridgecrest mainshock as estimated in real time at CWU (colored time series) with postprocessed kinematic positioning using the Gipsy-Oasis software (Zumberge *et al.*, 1997) and precise satellite orbits and clocks provided by Jet Propulsion Laboratory, California Institute of Technology (black overlain time series). Postprocessed data analyzed by D. Mencin of UNAVCO, Inc. (Mattioli *et al.*, 2020). The color version of this figure is available only in the electronic edition.

estimate of the GNSS offsets for 48 hr solutions. Part of the discrepancy may therefore be real, in the sense that the 25 s offsets are smaller than those estimated from daily positions but similar in overall directions. It seems reasonable that some of this discrepancy may ultimately be attributed to either rapid afterslip along the fault zone or cumulative deformation caused by nearly 1000 aftershocks, of which 71 were M_w 4.0 or greater, over the 48 hr after the mainshock that contribute to the 48 hr offset estimate but not the 25 s estimate. A detailed modeling of time-dependent postseismic deformation is beyond the scope of this article.

DYNAMIC DISPLACEMENTS

Waveform shapes of the dynamic displacements as estimated in real time compare well with those estimated with postprocessed GNSS data. Figure 3 compares CWU's real-time positions for three components (north, east, vertical) of the two stations closest to the fault zone that contain the largest dynamic and static displacements (colored time series) with postprocessed PPP time series generated with the Gipsy-Oasis (GIPSY) analysis package (black overlaid time series) by UNAVCO, Inc. (Zumberge *et al.*, 1997; Mattioli *et al.*, 2020). For this comparison, the postprocessed solutions may be considered "truth," and the extent to which the real-time positions match the postprocessed positions indicates the accuracy of the real-time positioning. The waveforms agree, and the real-time positioning accurately captures the dynamic displacements seen in the postprocessed data, particularly in the first ~30 s after rupture origin time. Agreement between real-time and postprocessed static offsets also match reasonably well, but show more drift in the real-time measurements compared with the postprocessed.

Real-time GNSS waveforms are also well modeled by synthetic position seismograms calculated with f-k synthetics (Zhu and Rivera, 2002) using the Hadley–Kanamori 1D P- and S-velocity models for southern California (Hadley and Kanamori, 1977; Hutton *et al.*, 2010) and the USGS finite-fault distribution for rupture location and timing inverted from global seismic network observations (Hayes, 2017). Figure 4 shows a comparison of the real-time GNSS positions (black) overlain by f-k synthetics (blue) in absolute time aligned on the mainshock rupture origin time. The finite-fault synthetics capture much of the characteristics seen in the real-time GNSS time series. General arrival times are close, and waveform shapes are similar and often include subarrivals that appear to originate from the source, meaning such subarrivals do not appear in point-source synthetics but only appear after convolution with finite-fault rupture propagation through space and time. Static offsets are also similar between the real-time-estimated and synthetic predictions seen in the time series.

DISCUSSION

From a monitoring standpoint, the real-time Ridgecrest mainshock coseismic measurements are substantially equivalent to postprocessed dynamic waveforms and offsets, and suggests the GNSS monitoring system worked as designed. It is important to note that the stations shown here were obtained routinely, as a product of a system comprising nearly 800 stations spanning North America plus several hundred more from around the globe. This number is continuously expanding as GNSS networks proliferate, telemetry costs steadily decrease, and station data are increasingly shared for hazards mitigation applications (International Union of Geodesy and Geophysics [IUGG], 2015; LaBrecque *et al.*, 2019). The future could see this number increase by orders of magnitude. Although no platform has yet been created to incentivize the sharing of such data, current generation smartphones now track GNSS carrier phase and are also capable of precision positioning (Minson *et al.*, 2015). Although GNSS seismic monitoring will never replace conventional seismometers due to its vastly lower sensitivity, for large earthquakes (currently around M_w 6.5 and higher, depending on fault-network geometry, but dropping as global positioning precision improves) GNSS monitoring

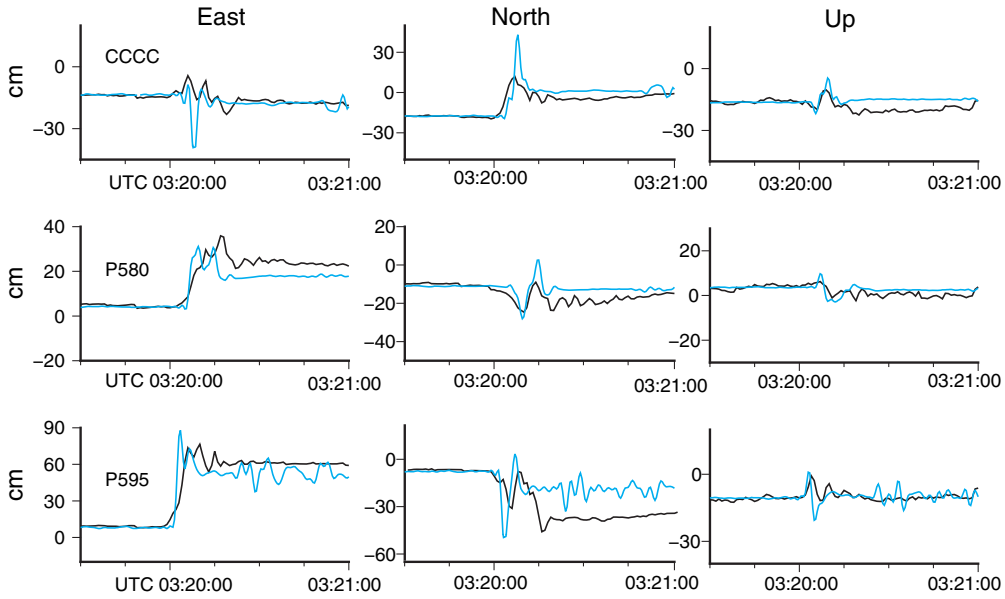

Figure 4. Comparison of mainshock ITRF14 real-time GNSS point position time series with synthetic position seismograms calculated using frequency–waveform Green's functions computed for the Hadley–Kanamori 1D velocity model for southern California (Hadley and Kanamori, 1977; Hutton *et al.*, 2010) and convolved with the U.S. Geological Survey (USGS) finite-fault slip distribution and time propagation (Hayes, 2017). Absolute travel times are aligned with respect to mainshock rupture OT at UTC 03:19:53. The color version of this figure is available only in the electronic edition.

can meaningfully contribute to traditional monitoring with seismometers, primarily for the larger events. GNSS coseismic offsets are readily converted to moment release through several approaches. For regions with sparse instrument coverage, simple displacement–moment scaling relationships allow moment to be quantified from a single station (Crowell *et al.*, 2013, 2016). For large earthquake near dense GNSS networks, finite-fault rupture may also be quantified as rupture propagates, and from this moment is easily quantified. However, because large earthquakes take longer to rupture than real-time positioning latency, coseismic deformation for large earthquakes takes significantly longer to converge than real-time latency. Nonetheless, coseismic offsets for the M_w 7.1 mainshock were generated in under half a minute.

In the context of earthquake early warning and ShakeAlert, it is worth noting that ultrafast determination of GNSS coseismic offsets could not have helped ShakeAlert improve its initial magnitude assessment, which, by necessity for maximizing warning time, must be made in the first several seconds after initial seismic detection. However, GNSS offsets, as they evolved, produced within the peak ground displacement moment scaling relationship of Crowell *et al.* (2013) conducted ex post facto using the nine stations shown in Figure 2, a magnitude of 6.9 within 14 s of rupture origin time (Crowell *et al.*, 2019). While not perfect, both the 14 s estimate, as well as the 25 s determination of static deformation, were obtained well before *S* waves first reached the densely populated Los Angeles basin, as shown in Figure 5. Neither the M_w 6.9 magnitude estimate at 14 s nor deformation at 25 s could have altered ShakeAlert decision making to alert within the 14 or 25 s circles, respectively, but both were quick enough to have potentially impacted the ultimate choice to not alert the Los Angeles Basin. This highlights how GNSS may be put to use to improve initial magnitude estimation for large events whose rupture duration and extent preclude accurate assessment using only the first few seconds of *P*-wave amplitudes, as discussed previously in Minson *et al.* (2014), Ruhl *et al.* (2017), Given *et al.* (2018), and Murray *et al.* (2018). The revised ShakeAlert Technical Implementation Plan (Given *et al.*, 2018) specifies that GNSS may be used to guide the issuance of revised warnings as faulting grows throughout and beyond the time window of initial, seismometer-based characterization. Although GNSS might have proven useful for better characterizing this event, with nearly 1000 real-time GNSS stations spanning the ShakeAlert footprint (Fig. 2, inset), few large future western U.S. earthquakes will escape detection by today's GNSS networks.

Finally, we note the lower limit of GNSS solution latency appears to be near 0.6 s, which is probably a better number to use for ShakeAlert algorithm design. Precise timing diagnostics conducted on the many steps in data transmission and analysis at CWU has shown that roughly 0.9 s of CWU's total solution latency arises from inefficient data transmission standards that handle the receipt of raw GNSS data. Preliminary testing employing several hundred stations over a one week period using an improved transmission protocols reduced overall latencies from just under 1.5 to 0.6 seconds. Planned upgrades to CWU's operational analysis system should yield these lower latencies in future routine operations.

DATA AND RESOURCES

Global Navigational Satellite System (GNSS) data used in this study were collected as part of the Network of the Americas operated by UNAVCO, Inc. Receiver Independent Exchange (RINEX) format data may be retrieved from www.unavco.org/data/gps-gnss/data-access-methods/data-access-methods.html (last accessed November 2019). Figures were generated with Gnuplot and Generic Mapping Tools

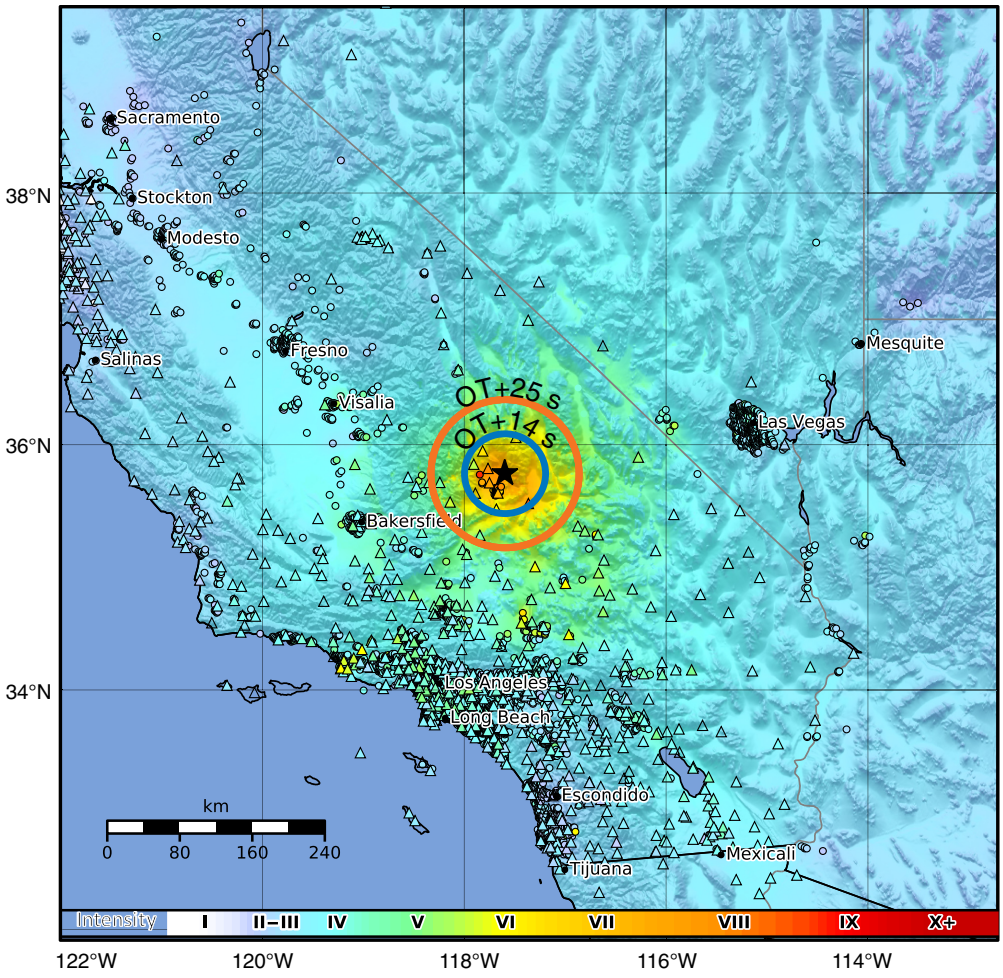

Figure 5. Areal extent of strong ground motion for which real-time GNSS-determined coseismic deformation and magnitude estimation could (area outside of circles) and could not (area inside of circles) assist in ShakeAlert decision making. Red circle shows strong ground motion propagation front at the time of convergence of coseismic deformation estimation filters (mainshock OT + 25 s); blue circle shows strong ground motion propagation front at the time peak-ground-displacement-based magnitude estimation convergence of M_w 6.9 (Crowell *et al.*, 2019). Propagation fronts are calculated at 3.2 km/s and overlain on USGS ShakeMap for the M_w 7.1 mainshock (Wald *et al.*, 1999); triangles show seismic instruments, and small circles show reported intensities. The color version of this figure is available only in the electronic edition.

(GMT). Supplemental material contains a gzipped tar file with time series in ASCII format, coseismic offset estimates in GMT format, and an Excel spreadsheet table of estimated offsets.

ACKNOWLEDGMENTS

All coauthors of this article contributed equal and complementary efforts. Development of Global Navigational Satellite System (GNSS) seismic analyses is supported by National Aeronautics and Space Administration (NASA)-Earth Surface and Interior (ESI) Awards NNX14AQ40G and 80NSSC19K0359 and U.S. Geological Survey (USGS) Cooperative Agreements G17AC00344 and G19AC00264 to Central Washington University. Data from Network of the Americas and postprocessed time series and coseismic offsets are provided by the Geodesy Advancing Geosciences and EarthScope (GAGE) Facility, operated by UNAVCO, Inc., with support from the National Science Foundation (NSF) and the NASA under NSF Cooperative Agreement EAR-1724794.

REFERENCES

Altamimi, Z., X. Collilieux, and L. Métivier (2011). ITRF2008: An improved solution of the international terrestrial reference frame, *J. Geodes.* **85,** 457–473.

Altamimi, Z., P. Rebischung, L. Métivier, and X. Collilieux (2016). ITRF2014: A new release of the International Terrestrial Reference Frame modeling nonlinear station motions, *J. Geophys. Res.* **121,** 6109–6131.

Barnhart, W. D., G. P. Hayes, and R. D. Gold (2019). The July 2019 Ridgecrest, California, earthquake sequence: Kinematics of slip and stressing in cross-fault ruptures, *Geophys. Res. Lett.* **46,** 11,859–11,867.

Crowell, B. W., M. A. Aranha, D. Smith, J. McGuire, J. R. Murray, A. I. Chung, N. M. Bartlow, S. E. Minson, C. J. Ruhl, C. Felizardo, *et al.* (2019). An analysis of source models and ground motion predictions from ShakeAlert geodetic and seismic algorithms for the Mw 7.1 Ridgecrest, CA earthquake, *American Geophysical Union Fall Meeting*, San Francisco, California, Paper Number S44C–03.

Crowell, B. W., D. Melgar, Y. Bock, J. S. Haase, and J. Geng (2013). Earthquake magnitude scaling using seismogeodetic data, *Geophys. Res. Lett.* **40,** 6089–6094.

Crowell, B. W., D. A. Schmidt, P. Bodin, J. E. Vidale, J. Gomberg, J. Renate Hartog, V. C. Kress, T. I. Melbourne, M. Santillan, S. E. Minson, *et al.* (2016). Demonstration of the Cascadia G-FAST geodetic earthquake early warning system for the Nisqually, Washington, earthquake, *Seismol. Res. Lett.* **87,** 930–943.

Dong, D., P. Fang, Y. Bock, M. K. Cheng, and S. Miyazaki (2002). Anatomy of apparent seasonal variations from GPS-derived site position time series, *J. Geophys. Res.* **107,** ETG 9-1–ETG 9-16.

Dow, J. M., R. E. Neilan, and C. Rizos (2009). The International GNSS Service in a changing landscape of Global Navigation Satellite Systems, *J. Geodes.* **83,** 191–198.

Given, D. D., R. M. Allen, A. S. Baltay, P. Bodin, E. S. Cochran, K. Creager, R. M. de Groot, L. S. Gee, E. Hauksson, T. H. Heaton,

et al. (2018). Revised technical implementation plan for the ShakeAlert system—An earthquake early warning system for the West Coast of the United States, *U.S. Geol. Surv. Open-File Rept. 2018-11*, Reston, Virginia.

Grapenthin, R., I. A. Johanson, and R. M. Allen (2014a). The 2014 Mw 6.0 Napa earthquake, California: Observations from real-time GPS-enhanced earthquake early warning, *Geophys. Res. Lett.* **41,** 8269–8276.

Grapenthin, R., I. A. Johanson, and R. M. Allen (2014b). Operational real-time GPS-enhanced earthquake early warning, *J. Geophys. Res.* **119,** 7944–7965.

Hadley, D., and H. Kanamori (1977). Seismic structure of the Transverse Ranges, California, *Geol. Soc. Am. Bull.* **88,** 1469–1478.

Hayes, G. P. (2017). The finite, kinematic rupture properties of great-sized earthquakes since 1990, *Earth Planet. Sci. Lett.* **468,** 94–100.

Herring, T. A., T. I. Melbourne, M. H. Murray, M. A. Floyd, W. M. Szeliga, R. W. King, D. A. Phillips, C. M. Puskas, M. Santillan, and L. Wang (2016). Plate Boundary Observatory and related networks: GPS data analysis methods and geodetic products, *Rev. Geophys.* **54,** 759–808.

Hodgkinson, K. M., D. Mencin, C. Sievers, T. Dittman, K. Feaux, K. E. Austin, C. P. Walls, and G. S. Mattioli (2018). A real-time GNSS Network of the Americas, *American Geophysical Union Fall Meeting*, San Francisco, California, Paper Number IN42B–04.

Hudnut, K. W., G. J. Anderson, A. Aspiotes, N. E. King, and K. F. Stark (2002). GPS fault slip sensors in earthquake alert systems, *American Geophysical Meeting Fall Meeting*, San Francisco, California, Paper Number G52A–0956.

Hutton, K., J. Woessner, and E. Hauksson (2010). Earthquake monitoring in Southern California for seventy-seven years (1932-2008), *Bull. Seismol. Soc. Am.* **100,** 423–446.

International Union of Geodesy and Geophysics (IUGG) (2015). Resolution 4: Real-time GNSS augmentation of the tsunami early warning system, *Proc. of the XXVI General Assembly*, Prague, Czech Republic, 22 June–2 July 2015.

Kong, L. S. L., P. K. Dunbar, N. s. Arcos, and , and International Tsunami Information Center (2015). *Pacific Tsunami Warning System: A Half-Century of Protecting the Pacific 1965–2015*, International Tsunami Information Center, Honolulu, Hawaii.

Kouba, J., and P. Héroux (2001). Precise point positioning using IGS orbit and clock products, *GPS Solutions* **5,** 12–28.

LaBrecque, J., J. B. Rundle, and G. W. Bawden (2019). Global navigation satellite system enhancement for tsunami early warning systems, *Global Assessment Report on Disaster Risk Reduction*, United Nations Office for Disaster Risk Reduction.

Litchfield, N., P. Villamor, R. J. V. Dissen, A. Nicol, P. M. Barnes, D. J. A. Barrell, J. R. Pettinga, R. M. Langridge, T. A. Little, J. J. Mountjoy, *et al.* (2018). Surface rupture of multiple crustal faults in the 2016 M_w 7.8 Kaikōura, New Zealand, earthquake, *Bull. Seismol. Soc. Am.* **108,** no. 3B, doi: 10.1785/0120170300.

Mattioli, G. S., D. A. Phillips, K. M. Hodgkinson, C. Walls, D. J. Mencin, B. A. Bartel, D. J. Charlevoix, C. Crosby, M. J. Gottlieb, B. Henderson, *et al.* (2020). The GAGE data and field response to the 2019 Ridgecrest earthquake sequence, *Seismol. Res. Lett.* doi: 10.1785/0220190283.

Melgar, D., B. W. Crowell, T. I. Melbourne, W. M. Szeliga, M. Santillan, and C. W. Scrivner (2020). Noise characteristics of operational real-time high-rate GNSS positions in a large aperture network, *J. Geophys. Res.* doi: 10.1002/essoar.10501291.1.

Minson, S. E., B. A. Brooks, C. L. Glennie, J. R. Murray, J. O. Langbein, S. E. Owen, T. H. Heaton, R. A. Iannucci, and D. L. Hauser (2015). Crowdsourced earthquake early warning, *Sci. Adv.* **1,** no. 3, e1500036 doi: 10.1126/sciadv.1500036.

Minson, S. E., J. R. Murray, J. O. Langbein, and J. S. Gomberg (2014). Real-time inversions for finite fault slip models and rupture geometry based on high-rate GPS data, *J. Geophys. Res.* **119,** 3201–3231.

Murray, J. R., B. W. Crowell, R. Grapenthin, K. Hodgkinson, J. O. Langbein, T. Melbourne, D. Melgar, S. E. Minson, and D. A. Schmidt (2018). Development of a geodetic component for the U.S. West Coast earthquake early warning system, *Seismol. Res. Lett.* **89,** 2322–2336.

Ponti, D. J., J. L. Blair, C. M. Rosa, K. Thomas, A. J. Pickering, S. Akciz, S. Angster, J. P. Avouac, J. Bachhuber, S. Bacon, *et al.* (2020). Documentation of surface fault rupture and ground deformation features produced by the Ridgecrest M6.4 and M7.1 earthquake sequence of July 4 and 5, 2019, *Seismol. Res. Lett.*, doi: 10.1785/0220190322.

Ross, Z. E., B. Idini, Z. Jia, O. L. Stephenson, M. Zhong, X. Wang, Z. Zhan, M. Simons, E. J. Fielding, S.-H. Yun, *et al.* (2019). Hierarchical interlocked orthogonal faulting in the 2019 Ridgecrest earthquake sequence, *Science* **366,** 346–351.

Ruhl, C. J., D. Melgar, R. Grapenthin, and R. M. Allen (2017). The value of real-time GNSS to earthquake early warning, *Geophys. Res. Lett.* **44,** 8311–8319.

Santillan, V. M., T. I. Melbourne, W. M. Szeliga, and C. W. Scrivner (2013). A fast-convergence stream editor for real-time precise point positioning, *Annual Meeting of the American Geophysical Union*, San Francisco, California, Paper Number G53B–0930.

Senko, J. (2018). Slip estimation from real-time GPS in Cascadia, *Master's Thesis in Geological Sciences*, Central Washington University.

Wald, D., K.-W. Lin, K. Porter, and L. Turner (2008). ShakeCast: Automating and improving the use of ShakeMap for post-earthquake decision-making and response, *Earthq. Spectra* **24,** 533–553.

Wald, D. J., V. Quitoriano, T. H. Heaton, H. Kanamori, C. W. Scrivner, and C. B. Worden (1999). TriNet "ShakeMaps": Rapid generation of peak ground motion and intensity maps for earthquakes in Southern California, *Earthq. Spectra* **15,** 537–555.

Zhu, L., and L. A. Rivera (2002). A note on the dynamic and static displacements from a point source in multilayered media, *Geophys. J. Int.* **148,** 619–627.

Zumberge, J. F., M. B. Heflin, D. C. Jefferson, M. M. Watkins, and F. H. Webb (1997). Precise point positioning for the efficient and robust analysis of GPS data from large networks, *J. Geophys. Res.* **102,** 5005–5017.

Manuscript received 17 February 2020
Published online 16 June 2020